UDC 551.515.21

Development of Asymmetries in a Three-Dimensional Numerical Model of the Tropical Cyclone[1]

RICHARD A. ANTHES—*The Pennsylvania State University, University Park, Pa.*

ABSTRACT—Notable asymmetric features of an early experiment with a three-dimensional hurricane model were spiral bands of convection and large-scale asymmetries (eddies) in the outflow layer. Using an improved version of the model, we describe the formation and maintenance of these features in greater detail in this paper. The spiral bands in the model propagate cyclonically outward in agreement with bands in nature. The breakdown of symmetry into a chaotic pattern of eddies in the outflow region is shown to be the result of dynamic (inertial) instability, with the eddy kinetic energy derived from the kinetic energy of the azimuthal flow. This instability does not contribute to the overall intensification of the model storm, however.

We observe a curious anticyclonic looping of the vortex center in these experiments. This looping appears to be associated with asymmetries in the divergence pattern associated with the eddies in the outflow layer.

This paper also summarizes improvements made in the original version of the model. In contrast to the earlier model, the current version contains an explicit water vapor cycle. A staggered horizontal grid is used to provide a higher resolution in evaluating the pressure gradient forces. Some of the pragmatic assumptions made in the earlier model, notably those involving horizontal diffusion of heat and momentum, have been eliminated in the current version.

CONTENTS

1. Introduction ---- 461
2. Review of Model ---- 462
   a. Basic equations ---- 462
   b. Structure of the model ---- 462
   c. Vertical diffusion of momentum ---- 462
   d. Horizontal diffusion of heat and momentum ---- 463
   e. Time integration ---- 463
   f. Lateral boundary conditions ---- 463
   g. Parameterization of cumulus convection ---- 463
   h. Water vapor budget and nonconvective latent heat release ---- 464
   i. Air-sea exchange of sensible and latent heat ---- 465
   j. Initial conditions ---- 465
3. Experimental Results ---- 465
   a. Addition of explicit water vapor cycle ---- 465
   b. Increased horizontal resolution utilizing staggered horizontal grids ---- 466
   c. Structure of asymmetric hurricane ---- 467
   d. The development of the asymmetric stage ---- 469
   e. The initial perturbations ---- 470
   f. Role of dynamic instability in the development of the asymmetries ---- 470
   g. Eddy kinetic energy budget ---- 472
   h. Increase of sea temperature in one quadrant ---- 473
4. Summary and Conclusions ---- 474
Appendix ---- 474
Acknowledgments ---- 475
References ---- 475

1. INTRODUCTION

Although considerable success in hurricane modeling has been achieved with two-dimensional models (e.g., Yamasaki 1968, Ooyama 1969, Rosenthal 1970*b*, Sundqvist 1970), a complete understanding of the tropical cyclone's life cycle requires consideration of the full three-dimensional problem. A preliminary version of an isolated, asymmetric hurricane model (Anthes et al. 1971*a*, hereafter referred to as I) reproduced at least two prominent asymmetric features associated with natural storms: spiral bands of upward motion and fairly large-scale asymmetries in the outflow layer. However, detailed analysis and interpretation of these features were deferred until additional experiments with an improved version of the model could be carried out. Especially conspicuous among the deficiencies in the preliminary model were the low vertical (3 levels) and coarse horizontal (30 km) resolution, the absence of a water vapor cycle, and a very pragmatic treatment of the lateral mixing process for heat and momentum. The above deficiencies have now been substantially improved with the exception of the vertical resolution increase. In particular, improved horizontal resolution is attained through a staggering of the horizontal grid, an explicit water vapor cycle is added, and a formulation of the horizontal diffusion processes similar to that used by Smagorinsky et al. (1965) is adopted. In experiments with the improved version of the model, several relationships have emerged involving the development and interaction of the asymmetries. This paper examines in detail the development of the asymmetric features using the current version of the model. The effect of the changes in grid structure, treatment of water vapor, and horizontal mixing are also discussed.

Symmetric hurricane models (Ooyama 1968) have shown a strong relationship between model storm intensity and the sea-surface temperature. A symmetric model cannot, however, investigate the effect of sea-surface temperature

[1] Most of this work was completed while the author was affiliated with the National Hurricane Research Laboratory, NOAA, Coral Gables, Fla.

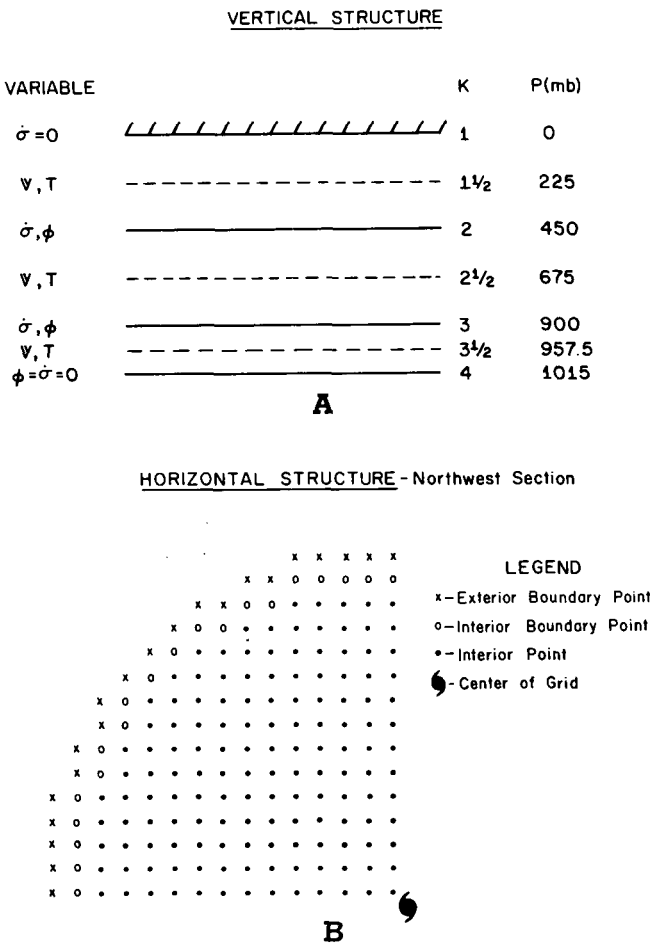

FIGURE 1.—(A) vertical information levels and (B) northwest quadrant of horizontal grid (nonstaggered).

variations on storm movement. A simple experiment is made to determine the effect of variations in sea temperature on the looping motion of the storm.

2. REVIEW OF MODEL

a. Basic Equations

The equations of motion are written in σ-coordinates (Phillips 1957) on an f-plane, where f, the Coriolis parameter, is appropriate to approximately 20°N ($5\times10^{-5}\mathrm{s}^{-1}$). The equations of motion, continuity equation, thermodynamic equation, and hydrostatic equation are identical to those employed by Smagorinsky et al. (1965) for general circulation studies. The basic equations are given in I and are not repeated here.

b. Structure of the Model

The vertical structure of the model is shown by figure 1A. The atmosphere is divided into upper and lower layers of equal pressure depth and a thinner Ekman boundary layer. The information levels for the dynamic and thermodynamic variables are staggered according to the scheme used by Kurihara and Holloway (1967).

Three horizontal grids are tested in the experiments discussed in this paper in an effort to economically achieve an increase in the horizontal resolution. The first is the grid utilized in I, in which all the variables are defined at all gridpoints. Two staggered horizontal grids are tested and shown to provide for a better resolution of the pressure gradient forces. These grids, and their associated finite-difference equations, are discussed in subsection 3b.

c. Vertical Diffusion of Momentum

As in the preliminary version of the model, the vertical diffusive and "frictional" effects are due to the vertical transports of horizontal momentum by subgrid eddies smaller than the cumulus scale. The most important aspect of these effects is the surface drag, which produces frictional convergence in the cyclone boundary layer and, therefore, a water vapor supply that controls the parameterized cumulus convection (Charney and Eliassen 1964, Ooyama 1969, Rosenthal 1970*b*).

In vector notation, these terms are written for the σ-system

$$\mathbf{F}_v=-g\frac{\partial\boldsymbol{\tau}^z}{\partial\sigma} \tag{1}$$

where g is the acceleration of gravity and $\boldsymbol{\tau}^z$ is the vector Reynolds stress. The quadratic stress law, with the surface wind speed approximated by the speed at level 3, is employed for the stress at $\sigma=1$; that is,

$$\boldsymbol{\tau}^z_{k=4}=\rho^*C_D|\mathbf{V}_3|\mathbf{V}_3 \tag{2}$$

where $\mathbf{V}$ is the horizontal wind vector. A value of 3×10^{-3} is adopted for the drag coefficient, C_D, and a standard value of $1.10\times10^3\ \mathrm{kg\cdot m^{-3}}$ is used for the surface density, ρ^*, in eq (2). As an upper boundary condition,

$$\boldsymbol{\tau}^z_{k=1}=0. \tag{3}$$

For the remaining σ-levels,

$$\boldsymbol{\tau}^z_{k=2,3}=\rho(z)\mu(z)\frac{\partial\mathbf{V}}{\partial z}. \tag{4}$$

Here, $\rho(z)$ is density, z is height, and $\mu(z)$ is the kinematic coefficient of eddy viscosity.

Following Smagorinsky et al. (1965), $\mu(z)=l^2|\partial\mathbf{V}/\partial z|$ where l is the mixing length. In this model, l need only be assigned at levels 2 and 3. In the preliminary report, l varied linearly from a maximum value of 35.5 m at level 3 to 0 at level 1, yielding a value of 17.8 m at level 2. In later experiments, the values of $\mu(z)$ at levels 2 and 3 were increased by an order of magnitude to reduce what subjectively appeared to be excessive vertical shear. The form currently in use for $\mu(z)$ is

$$\mu(z)=25+\alpha^2\left|\frac{\partial\mathbf{V}}{\partial z}\right| \qquad (\mathrm{m^2/s}) \tag{5}$$

with $\alpha^2=4\times10^4\ \mathrm{m^2}$. The value of $\mu(z)$ computed from eq (5) is about 20 times the value of $\mu(z)$ computed in the original experiment at level 3 and about 40 times the original value at level 2 during the mature stage of development.

We recognize that the form of $\mu(z)$ given by eq (5) is, at best, a temporary representation of the total effect

of vertical mixing of momentum in the hurricane, because cumulus clouds having the same vertical scale as the hurricane itself play an important role in the vertical transfer of momentum. However, this formulation yields an order of magnitude of $\mu(z)$ (50–100 m^2/s) found to give vertical shears representative of real hurricanes in symmetric models (Rosenthal 1970*a*, Anthes 1971*b*). It is noteworthy that experiments with the symmetric analog (Anthes et al. 1971*c*) show that the exact form of $\mu(z)$ above the boundary layer is relatively unimportant. Finally, the finite-difference expression for the vertical "frictional" force is

$$\mathbf{F}_v = -g\frac{\delta\tau^z}{\delta\sigma}, \tag{6}$$

where the vertical differencing operator, δ, is defined in the appendix.

d. Horizontal Diffusion of Heat and Momentum

The lateral exchange of horizontal momentum, F_H, by subgrid scale eddies given by Smagorinsky et al. (1965) is

$$F_H(\mathbf{V}) = \frac{\partial}{\partial x}\left(K_H\frac{\partial p^*\mathbf{V}}{\partial x}\right) + \frac{\partial}{\partial y}\left(K_H\frac{\partial p^*\mathbf{V}}{\partial y}\right). \tag{7}$$

The formulation of K_H in I, based on early tests and on results from symmetric model experiments (Rosenthal 1970*a*), was

$$K_H = C_1|\mathbf{V}| + C_2 \tag{8}$$

where $C_1 = 10^3$ m and $C_2 = 5\times10^3$ m^2/s. The current version of the model, however, utilizes a nonlinear form similar to that used by Smagorinsky et al. (1965),

$$K_H = 5\times10^3 + \frac{k_0^2}{2}(\Delta S)^2|D| \tag{9}$$

where ΔS is the grid spacing (30 km),

$$D = \left[\left(\frac{\partial u}{\partial x} - \frac{\partial v}{\partial y}\right)^2 + \left(\frac{\partial v}{\partial x} + \frac{\partial u}{\partial y}\right)^2\right]^{1/2}, \tag{10}$$

and k_0, the von Kármán constant, equals 0.4. In eq (9), the constant part is important only near the outer boundary where the kinetic energy and horizontal shear are small.

For simplicity, the diffusion of heat in the original version of the model was modeled using a constant thermal diffusivity,

$$F_H(T) = p^*\left[\frac{\partial}{\partial x}\left(K_T\frac{\partial T}{\partial x}\right) + \frac{\partial}{\partial y}\left(K_T\frac{\partial T}{\partial y}\right)\right], \tag{11}$$

with K_T chosen by trial and error to be 5×10^4 m^2/s. In the current version of the model, however, the diffusivities for heat, momentum, and water vapor are equal to K_H computed from eq (9).

e. Time Integration

As in I, the Matsuno (1966) simulated forward-backward scheme is utilized for the time integration. This scheme damps the very high frequency gravity waves without significantly damping the low and medium frequencies. See I for details.

f. Lateral Boundary Conditions

The small domain size and the irregular boundary make the choice of lateral boundary conditions very important. In I, the components of momentum were extrapolated outward from interior gridpoints regardless of the direction of the flow. A subsequent experiment, however, produced a more intense storm than the preliminary model storm, and the extrapolation outward of the momentum in areas of inflow led to an instability in which a rather intense jet formed near the boundary. The source of energy for this jet was apparently the unlimited supply of kinetic energy from the environment. In subsequent experiments, therefore, the momentum components on the boundary are extrapolated only where the normal flow is outward. For inflow, the momentum on the boundary is set to zero.

As in I, the boundary values for pressure and temperature are in uniform steady state. In experiments that include an explicit water vapor cycle, the relative humidity on the boundary is fixed at 90 percent.

g. Parameterization of Cumulus Convection

A major improvement in the model experiments discussed in this paper is the addition of an explicit water vapor cycle. This change eliminates the assumptions concerning boundary layer water vapor content that were necessary in I and allows for simulation of nonconvective release of latent heat. This section describes the parameterization of the feedback between convection and the large-scale temperature and moisture fields. The following section describes the water vapor cycle and the nonconvective release of latent heat. Nonconvective release of latent heat is defined as the latent heat released in a conditionally stable column in which the precipitation results from steady, stable ascent of saturated air. The flow chart for both schemes is summarized in figure 2.

The parameterization of the cumulus convection closely follows the scheme used successfully by Rosenthal (1970*b*), although some slight modifications are necessary because of the reduced vertical resolution. The basic characteristics of the scheme have been thoroughly discussed elsewhere (Rosenthal 1969, 1970*a*) and will not be elaborated upon here. The two most important aspects of the scheme may be summarized, however:

1. In the convective parameterization, the vertical integral of latent energy is conserved.
2. The heat and moisture made available to the environment are distributed vertically in such a way that the environment is driven toward an ultimate state in which the humidity and temperature are those defined by the equivalent potential temperature of the surface air.

The convective adjustment for the σ-system is

$$I = \frac{\nu}{\sum_{k=1}^{3}\left[(T_c - T)\frac{c_p}{L} + (q_c - q)\right]\delta\sigma_k} \tag{12}$$

where T_c and q_c are the temperature and specific humidity, respectively, of the pseudo-adiabat with the equivalent potential temperature of the surface, q and T are the environmental specific humidity and temperature, respectively, L is the latent heat of vaporization, and c_p is the specific heat for dry air at constant pressure. The term ν combines the boundary layer convergence of water vapor and the latent heat addition from the sea, Q_{sea}; that is,

$$\nu = -\nabla \cdot p^* \mathbf{V} q_3 \delta\sigma_3 + Q_{\text{sea}}. \tag{13}$$

If $\dot{Q}_c$ is that part of the diabatic heating due to convection, then

$$p^* \dot{Q}_c \begin{cases} = c_p I (T_c - T) & \text{if } (T_c - T) \geq 0.5°\text{C} \\ & \text{and } I > 0 \\ = 0 & \text{otherwise.} \end{cases} \tag{14}$$

If we let $(\partial q p^*/\partial t)_c$ represent the addition of moisture to the environment by cumulus convection, then

$$\frac{\partial q p^*}{(\partial t)_c} \begin{cases} = I(q_c - q) & \text{if } I(q_c - q) > 0 \\ & \text{and RH} \leq 98 \text{ percent} \\ = 0 & \text{otherwise.} \end{cases} \tag{15}$$

Equations (12)–(15) are used only when the atmosphere is conditionally unstable; that is, when $(T_c - T)$ and $(q_c - q)$ are positive for some value of k. To avoid numerical difficulties with small values of the denominator of eq (12), we assume that convection occurs only if $(T_c - T)$ equals or exceeds 0.5°C at either level 1½ or 2½. As an additional constraint on the vertical partitioning of latent heat under nearly moist neutral conditions ($T_c \approx T$ and $q_c \approx q$), an arbitrary upper limit of 20 percent of the total latent heat in the column is assigned to the boundary layer (level 3½), and the remaining 80 percent is distributed between the middle and upper tropospheric layers.

An additional modification to the above scheme occurs in a nearly saturated environment, defined by a relative humidity (RH) equal to or greater than 98 percent. Under these conditions, $(\partial q p^*/\partial t)_c$, which may be thought of as resulting from evaporating clouds, is set equal to zero, and all of the condensation heating is made available to the large-scale flow. The precise choice of 98 percent is relatively unimportant; a limit somewhat less than 100 percent was chosen to avoid sporadic addition of this source when the large-scale relative humidity oscillates about the 100-percent value. This latter oscillation is presumably the result of the addition of temperature and moisture increments associated with the finite differencing.

The surface temperature, T^*, needed to establish the surface equivalent potential temperature, is computed by a downward extrapolation from level 3½; that is,

$$T^* = T_{3\frac{1}{2}} + 3.636°\text{K}, \tag{16}$$

and the surface specific humidity is obtained by the assumption that the relative humidity at the surface equals the humidity at $k = 3\frac{1}{2}$.

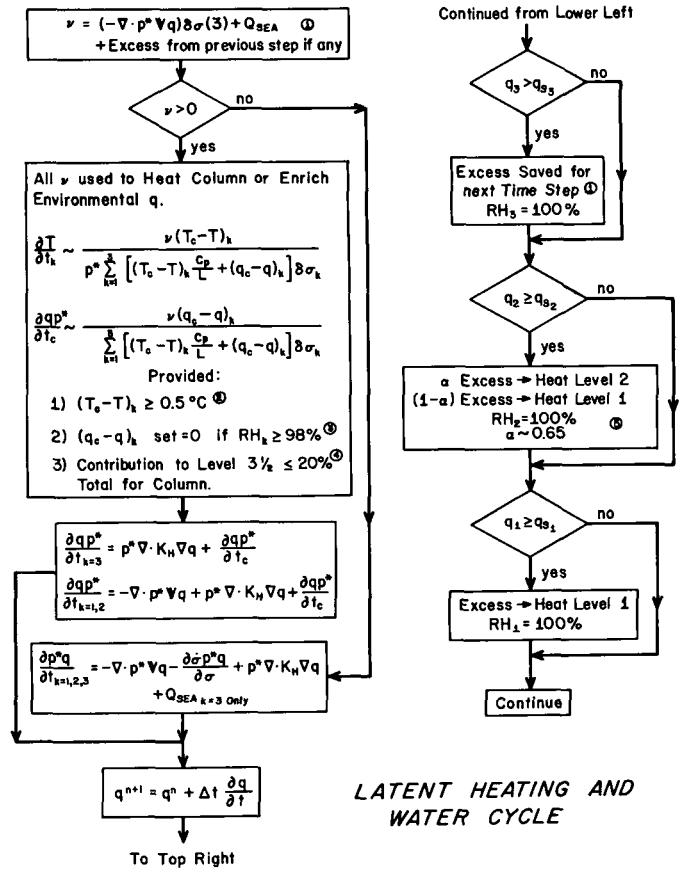

FIGURE 2.—Flow chart illustrating water vapor cycle and parameterization of convective and nonconvective latent heat release. See subsections 2g and 2h for details.

h. Water Vapor Budget and Nonconvective Latent Heat Release

The treatment of the water vapor cycle closely follows the scheme developed by Rosenthal (1970*b*) for the symmetric, seven-level model, again with some modifications due to its limited vertical resolution. The scheme is outlined in figure 2.

Under unsaturated conditions in the presence of convection, all of the boundary layer water convergence and the evaporation from the sea is utilized in convection, and the forecast equation for specific humidity at level 3½ is simply

$$\frac{\partial p^* q}{\partial t} = p^* \nabla \cdot K_H \nabla q + \left(\frac{\partial p^* q}{\partial t}\right)_c. \tag{17}$$

In the middle and upper layers, the forecast equation is

$$\frac{\partial p^* q}{\partial t} = -\nabla \cdot \mathbf{V} p^* q + p^* \nabla \cdot K_H \nabla q + \left(\frac{\partial p^* q}{\partial t}\right)_c. \tag{18}$$

In columns which contain no convection, the forecast equation is

$$\frac{\partial p^* q}{\partial t} = -\nabla \cdot p^* \mathbf{V} q - p^* \frac{\partial \dot{\sigma} q}{\partial \sigma} + p^* \nabla \cdot K_H \nabla q + Q_{\text{sea}} \tag{18a}$$

where the term Q_{sea} represents evaporation from the sea surface (subsec. 2i). The interpolation of q to the $\dot{\sigma}$ levels necessary for computing the vertical flux in eq (18a) is

obtained by assuming an exponential variation of q between the σ-levels,

$$q=q_0e^{k(p-p_0)} \tag{19}$$

where p is pressure and the reference level is designated by the subscript 0. Evaluating the constant, k, we obtain

$$\bar{q}_k=q_{k+1/2}\left(\frac{q_{k-1/2}}{q_{k+1/2}}\right)^{\left(\frac{\sigma_k-\sigma_{k+1/2}}{\sigma_{k-1/2}-\sigma_{k+1/2}}\right)} \tag{20}$$

and

$$\frac{\partial\dot{\sigma}q}{\partial\sigma}\approx\frac{\delta\dot{\sigma}\bar{q}}{\delta\sigma}. \tag{21}$$

The release of nonconvective latent heat is modeled in the following manner. After every forecast step, each gridpoint for specific humidity is checked for supersaturation. If supersaturation occurs in the boundary layer and conditional instability is still present, the water vapor excess over saturation is used to fuel additional convection according to the convective scheme given by eq (14) and (15). In the event (rare) that supersaturation occurs in the boundary layer and the atmosphere is conditionally stable, the excess moisture is condensed in situ.

For supersaturation at levels 1½ and 2½, the excess vapor is assumed to condense as large-scale precipitation rather than convection, since the atmosphere is conditionally stable above these levels. At level 1½, all the excess is condensed and the latent heat is made available to the circulation at this level. For supersaturation at level 2½, however, only part (65 percent) of the excess water vapor is condensed at this level; the remainder is assumed to condense at level 1½. This partitioning follows from the assumption that the mechanism for the latent heat release is large-scale ascent of saturated air. For typical hurricane soundings, a saturated parcel starting at level 2½ (about 675 mb) and rising to the tropopause condenses about 65 percent of its total water vapor below 450 mb (level 2) and the rest above this level.

i. Air-Sea Exchange of Sensible and Latent Heat

The sensible and latent heat fluxes at the air sea interface obey the bulk aerodynamic relationships and decrease linearly with σ until they reach zero at the $k=3$ level. This gives

$$p^*\dot{Q}_s=\begin{cases}\dfrac{gc_pC_E|\mathbf{V}|\rho^*(T_{sea}-T^*)}{\sigma_4-\sigma_3} & T_{\text{sea}}>T^*\\ 0 & T_{\text{sea}}\leq T^*\end{cases} \tag{22}$$

and

$$Q_{\text{sea}}=\begin{cases}\dfrac{gC_E|\mathbf{V}|\rho^*(q_{sea}-q^*)}{\sigma_4-\sigma_3} & q_{\text{sea}}>q^*\\ 0 & q_{\text{sea}}\leq q^*\end{cases} \tag{23}$$

where $\dot{Q}_s$ and Q_{sea} are the sensible and latent heat added per unit mass and time at level 3½. The exchange coefficient, C_E, is taken equal to C_D (0.003) and the value of T_{sea} is 302°K for most of the experiments. The effect of varying C_E, C_D, and T_{sea} have been investigated elsewhere with symmetric models (Ooyama 1969, Rosenthal 1971, Anthes 1972).

j. Initial Conditions

The initial conditions consist of an axisymmetric vortex in gradient balance, having a maximum wind speed of 18 m/s at a radius of 240 km. The details are presented in I. For initially symmetric conditions, the solutions to the *differential* equations remain symmetric for all time. However, asymmetries in the truncation and roundoff errors as well as in the lateral boundaries produce weak asymmetries (subsec. 3e) in the *finite-difference* equations after the first time step. These perturbations may then grow with time and become a significant part of the total circulation. In a later section, the mechanism for this observed growth is investigated. It is also shown that the initial form of the perturbation is unimportant in determining the final form of the asymmetries.

3. EXPERIMENTAL RESULTS

The next two subsections briefly describe the effects of the major modifications to the original version of the model, specifically, the addition of the water vapor cycle and the horizontal staggering of the grid. The details of the model storm structures associated with these intermediate stages of the model are not presented. Subsections 3c–3g present detailed analyses of the model storm's life history as computed from the current version of the model. These subsections are primarily concerned with the development and structure of the asymmetric features including rainbands and outflow eddies.

Table 1 lists some of the properties of each experiment discussed in this paper. These properties, appropriate to the mature stage of each model storm, serve as an overall comparison of the experiments and are discussed individually in later sections.

a. Addition of Explicit Water Vapor Cycle

Figure 3 shows the time variation of the minimum surface pressure and the maximum surface wind speed for each experiment. The effect of adding the explicit water vapor cycle alone is illustrated by the curves labeled "nonstaggered grid," and, as suggested by the close similarity to the corresponding profiles for experiment I, the water vapor cycle has a fairly small effect on the overall behavior of the model storm. The initial development is somewhat slower because part of the water vapor convergence in the boundary layer is used to enrich the environmental water vapor content in the middle and upper troposphere (the initial relative humidity at all levels is 90 percent). In experiment I, which does not contain a water vapor cycle, *all* the water vapor convergence is condensed and made available as latent heat to the large-scale flow.

Although the initial development in the experiment with the water cycle is slower, the ultimate state is equal to, or slightly greater than in experiment I. This difference is related to somewhat higher boundary-layer specific humidities in the later model. The structures of the two model experiments are quite similar and are not compared in detail. Therefore, the primary advantages of adding

467-299 O - 72 - 7

TABLE 1.—*Summary of experiments*

Experiment	Grid	Min p (mb)	Max V (m/s)	10^{14} W Total heating rate	Convective heating rate	Noncon-vective heating rate	Sensible heating rate	10^{12} W $C(K)$	D_H	D_V
1. Anthes et al. (1971*a*) (228 hr)*	Nonstaggered	965	66	13. 9	13. 9	—	0. 46	45	−11	−32
2. H_2O cycle added (282 hr)	Nonstaggered	962	66	11. 8	11. 4	0. 4	0. 24	43	−16	−28
3. Initial asymmetries, 10^{-11}% (174 hr)	S1	976	60	10. 0	8. 6	1. 4	0. 19	31	−10	−19
4. Initial asymmetries 10^{-1}% (120 hr)	S1	976	60	11. 2	9. 9	1. 3	0. 21	36	−11	−23
5. Aborted due to lateral boundary problems (87 hr)	S2	980	57	7. 2	6. 8	0. 4	0. 11	17	−7	−9
6. Nonlinear-type horizontal mixing (156 hr)	S1	971	63	12. 6	10. 6	2. 0	0. 22	36	−11	−24
7. Symmetric analog (96 hr)	1 horizontal dimension staggered grid	969	53	15. 1	12. 4	2. 7	0. 30	39	−11	−28

*Time in parentheses is time at which components of energy budget are given.

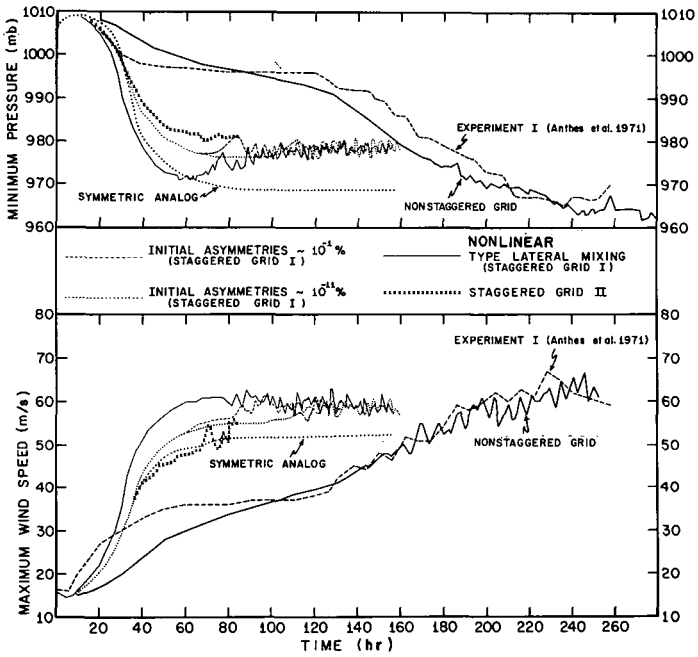

FIGURE 3.—Time variation of minimum pressure and maximum surface wind speed for experiments discussed in this paper.

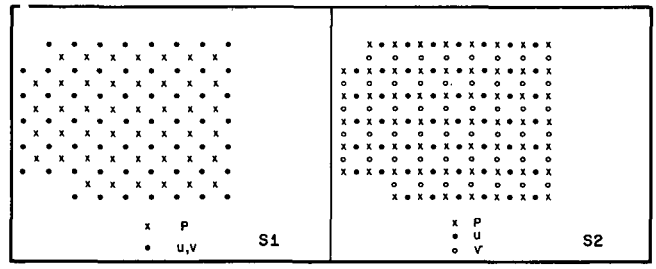

FIGURE 4.—Schematic diagram for two staggered horizontal grids tested with hurricane model. S1 grid is shown on left, S2 grid is shown on right.

the water vapor cycle are: (1) the elimination of some arbitrary assumptions made in the first experiment, (2) the provision for a wider range of initial conditions (variations in initial humidity distributions), and (3) the provision for studying the hurricane water vapor budget.

b. Increased Horizontal Resolution Utilizing Staggered Horizontal Grids

The behavior of the two experiments utilizing the nonstaggered grid are more similar to each other than to any of the other experiments shown in figure 3. More significantly, during the early stages of the storms when asymmetries are negligible, the behavior of the nonstaggered-grid storms varies markedly from the behavior of the symmetric analog (Anthes et al. 1971*c*). From their comparison of the asymmetric and symmetric models, Anthes et al. concluded that the differences during the early stages of the storm were related to greater truncation errors in evaluating the pressure gradient force in the asymmetric model. The symmetric analog, which utilized a staggered grid in the radial direction to avoid computational difficulties at the origin, evaluated the pressure gradient over 30 km rather than over the 60-km interval used by the asymmetric model. The comparison suggested a staggering of the pressure and velocity variables in the asymmetric model as well.

The staggering of variables in two horizontal dimensions is somewhat more complicated than in one dimension. Two types of staggered grids, shown schematically in figure 4, were tested. The first (designated by S1) consists of two sets of prediction points, one for the horizontal velocity components and one (offset by 45°) for all the other variables. The second (designated by S2) consists of three sets of prediction points, one for each horizontal velocity component and a third for the remaining variables. The S2 grid has been used by Lilly (1965) and tested by Grammeltvedt (1969). In both staggered grids, the evaluation of the pressure gradient and the horizontal divergence over smaller grid increments neces-

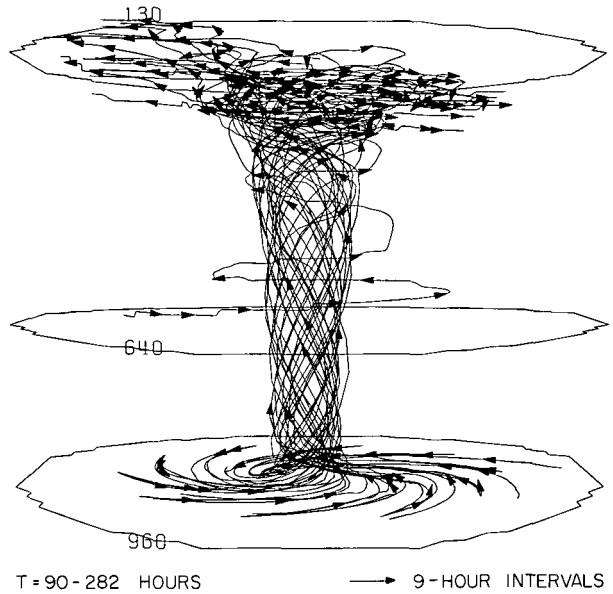

FIGURE 5.—Particle trajectories calculated over a 9-day period in experiment 2 (table 1). The three levels are labeled in millibars (approximate). All particles start in the boundary layer except one, which is started in the middle troposphere.

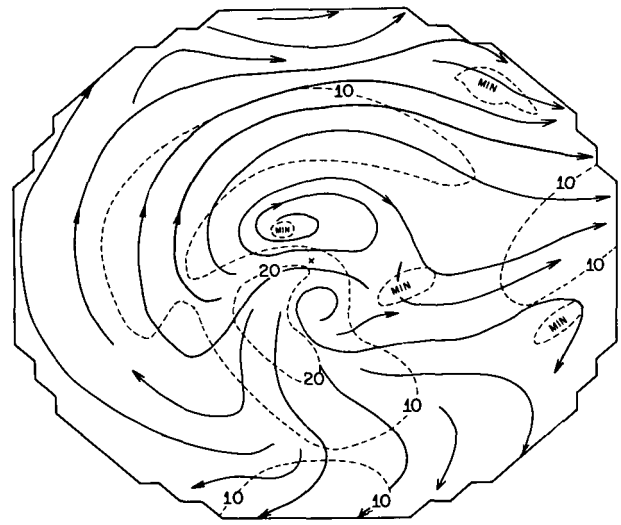

FIGURE 6.—Streamline and isotach (m/s) analysis for level 1½ in experiment 6 (table 1) during the mature asymmetric stage (156 hr).

sitates a reduction in the time step to maintain computational stability. Thus, the time step of 60 s that was adequate for the nonstaggered grid must be reduced to 45 s for S1 and to 30 s for S2. The alternate finite-difference equations associated with each staggered grid are given in the appendix.

As seen in figure 3, both staggered grids yield very similar results during the first 48 hr of model time. Furthermore, both experiments are more similar to the symmetric analog than are the two experiments with the unstaggered grid. The solutions associated with the S1 and S2 grids diverge considerably after 48 hr, however, with the S2 storm reaching an asymmetric stage much earlier than the S1 storm. Furthermore, the solution associated with the S2 grid deteriorates after 72 hr and finally becomes unstable. The primary cause of this instability seems to be associated with the lateral boundary conditions, since the u and v components are not defined at the same points. This instability and the requirement for the small time step were the prime reasons for the choice of the S1 grid for the current version of the model. The S1 grid, then, provides for an economical increase in horizontal resolution, and the behavior of the symmetric stage of the model storm utilizing this grid compares favorably with the behavior of the symmetric analog.

c. Structure of Asymmetric Hurricane

The structures of the storms generated in the later experiments are similar to the storm structure discussed in I. An overall view of the three-dimensional, time-dependent structure of a typical experiment (experiment 2, table 1) is shown in figure 5, which shows the tracks of particles released in the hurricane circulation over an 8-day period. The computed velocities are interpolated in space and time for the computation of the trajectories. See Anthes et al. (1971*b*) for more details. Figure 5 reveals a nearly steady state, axisymmetric boundary layer in which air accelerates as it flows inward to the center. Reaching the center, the particles are carried rapidly upward, reaching the outflow layer in about 2 hr. (Note that the large-scale, mean vertical velocities are used to compute the vertical displacements; in reality, a particle would probably be carried upward in a cumulonimbus updraft in considerably less time.) After the particles reach the outflow layer, they decelerate and move outward in a highly asymmetric, unsteady flow.

Figure 5 also shows the path of one particle that is released in the middle troposphere (about 500 mb) rather than in the inflow layer. This particle experiences very little radial motion and is carried slowly upward as it spirals around the storm center.

Figure 6 shows a typical streamline and isotach pattern in the upper level during the mature stage (156 hr) of experiment 6. Noteworthy is the anticyclonic eddy located to the "north" of the storm center. The outflow occurs mainly in two jets, in agreement with storms in nature (Black and Anthes 1971).

The temperature structure in experiment 6 (not shown) is relatively symmetric compared to the winds. The maximum temperature excess over the undisturbed environment is 7°–8°C in the revised version of the model compared to the excess of 3°–4°C found in the preliminary experiment I. This higher figure, which is apparently due to the effective increase in horizontal resolution, is still somewhat lower than observations (Hawkins and Rubsam 1968) and multilevel symmetric models (Rosenthal 1970*b*) indicate. However, the lower figure is considered reasonable in view of the great depth of the tropospheric outflow layer necessitated by the low vertical resolution.

Figure 7 shows the vertically integrated convective heat release, expressed as cm of rain per day. The semicircle of rainfall rates over 200 cm/day corresponds well to the nonuniform eyewall convective region in real storms

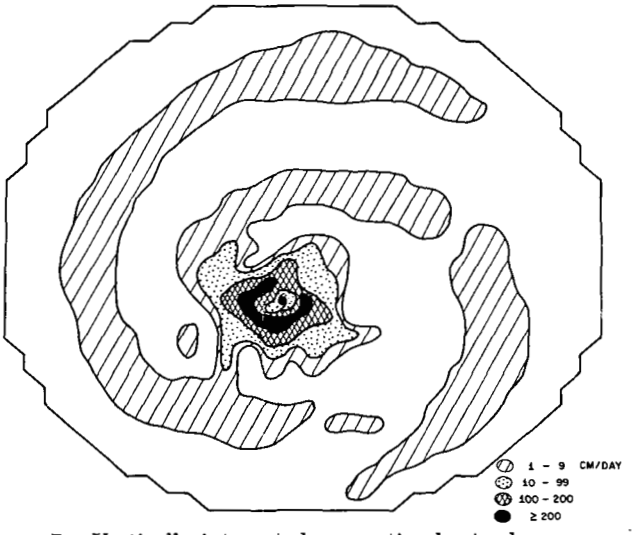

FIGURE 7.—Vertically integrated convective heat release expressed as rainfall rates (cm/day) at 156 hr of experiment 6.

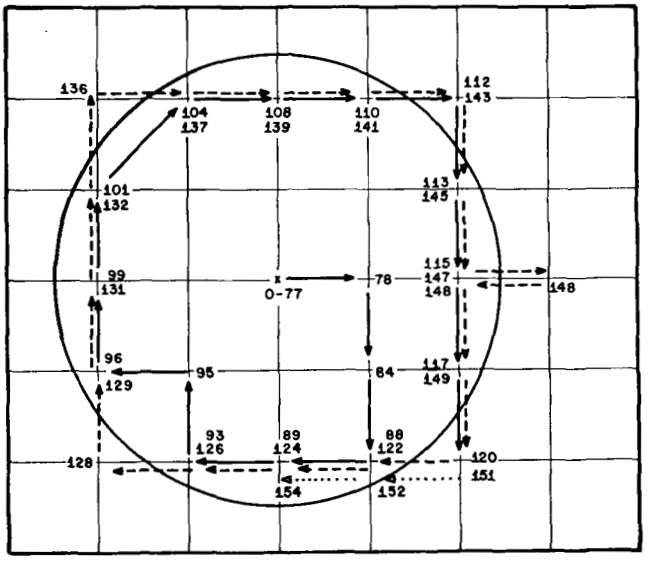

FIGURE 8.—Positions of minimum pressure at selected times (hr) for experiment 6 (table 1) showing anticyclonic looping during asymmetric stage of storm. Speed of rotating center is approximately 4.1 m/s.

(e.g., Hawkins and Rubsam 1968). However, figure 7 shows that a rain-free "eye" is not present at this time, and only a region of relatively light rainfall occurs at the center of the storm. The absence of an eye is probably due to the coarse horizontal resolution. The notable spiral bands, with rainfall rates averaging about 2 cm/day, are approximately 90 km wide at large distances from the center and somewhat wider closer to the center. These bands rotate cyclonically about the storm center and propagate outward at a speed [2] of about 24 kt. Although the outer rainbands in nature apparently propagate outward (Gentry 1964, Senn and Stevens 1964), we feel that the model rate of 24 kt is somewhat too high. Since the bands are undoubtedly internal gravity waves, improved vertical resolution may give a more realistic phase speed. The band thickness of 90 km is considered fairly acceptable compared to observations, when the coarse resolution of the model is considered. The rainfall rate of 2 cm/day is also considered acceptable, although possibly on the low side, for an average over 60 km.

The temperatures inside the bands are not appreciably different from the surrounding environment, in agreement with the mean thermal structure of outer bands in nature (Gentry 1964). This uniformity in temperature may be related to the near compensation in the thermodynamic equation between the latent heat release and the adiabatic cooling in the region of upward motion and to the relatively short time (about 3 hr) required for the band to move past a particular point. It is noteworthy that, compared to earlier versions of the model, the current version yields spiral bands with the structure most like rainbands in nature.

Although the spiral bands in the model are undoubtedly internal gravity waves modified by latent heat release (Ogura and Charney 1962), the mechanism for their generation is unknown. There does seem to be an interesting, although obscure, relationship between the bands, which are most pronounced at the top of the boundary layer, and the asymmetries in the outflow layer. In all experiments, the bands are conspicuously absent until the symmetric flow in the upper levels breaks down. Also, the number of bands (two) seems to be associated with the predominance of wave number 2 in the outflow layer.

The release of latent heat in the spiral bands is entirely convective. Charney (1971) suggests that the conditional instability of the second kind (CISK) process (Charney and Eliassen 1964) may be relevant in describing the cumulus–rainband scale interactions as well as the cumulus–cyclone scale interactions To investigate this possibility, one needs further experiments with increased resolution to permit meaningful estimates of the vorticity and energy budgets of the rainbands.

The nonconvective latent heat release (not shown) occurs entirely within 180 km of the center in a roughly circular pattern. The total nonconvective heat release of 2.0×10^{14} W (table 1) represents a significant contribution to the total latent heat release (12.6×10^{14} W), in agreement with observations (Hawkins and Rubsam 1968) and symmetric model results (Rosenthal 1970*b*).

A curious feature of the later experiments, which was not present in I, is an anticyclonic looping of the vortex center about the center of the grid. Figure 8 shows the path for experiment 6, which approximates a circle of 75-km radius. The commencement of the looping is coincident with the formation of outflow asymmetries, suggesting that the eddies that drift with the anticyclonic flow of the upper levels are controlling the looping of the vortex center. It is possible that the lateral boundaries are responsible for the tight, circular looping, and with a much larger domain the vortex center might meander in a less organized pattern.

The time variation of the mass-integrated total kinetic energy budget for experiment 6 is shown in figure 9. The

[2] This speed is computed by measuring the normal displacement of the outer edge of the bands over a 6-hr period and hence includes the effect of rotation as well as outward propagation.

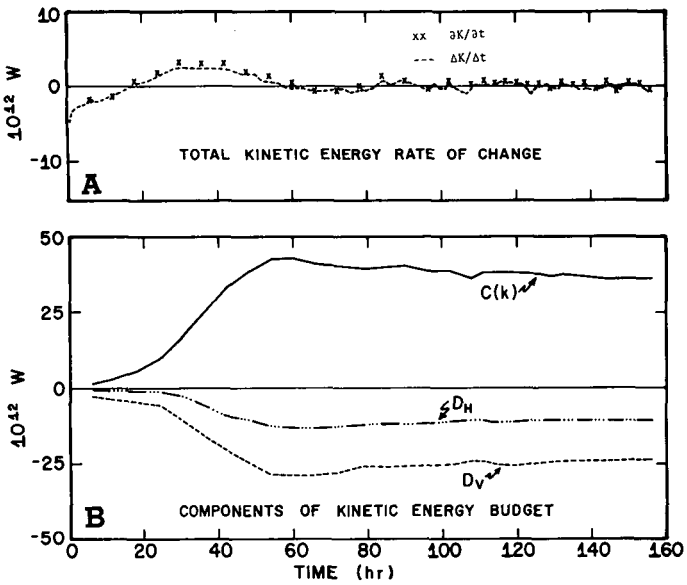

FIGURE 9.—(A) time variation of the observed total kinetic energy change ($\Delta K/\Delta t$) and the change computed from the kinetic energy equation ($\partial K/\partial t$) for experiment 6 and (B) individual components of the kinetic energy tendency. $C(K)$ is the conversion of potential to kinetic energy, D_H is the dissipation of kinetic energy through lateral eddy viscosity, and D_V is the dissipation of kinetic energy through vertical eddy viscosity and includes the effect of surface drag friction. The flow of kinetic energy through the lateral boundary is negligible in this experiment.

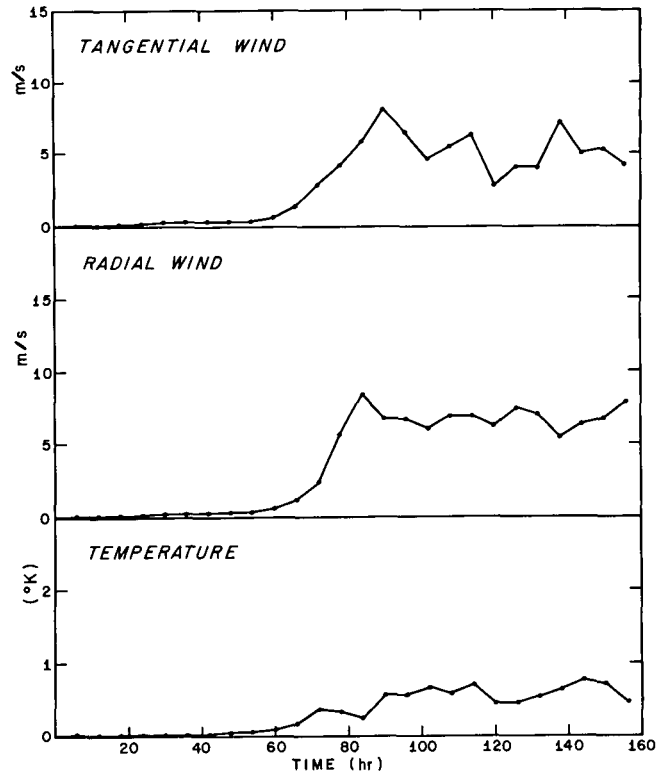

FIGURE 10.—Time variation of standard deviations of tangential and radial wind components and temperature for the upper level at a radius of 105 km in experiment 6.

kinetic energy equation for this model is presented in I. The difference between the observed kinetic energy rate of change and the tendency computed from the kinetic energy equation is small. (See fig. 9A.) This close agreement indicates that truncation errors in the model, including those associated with the time integration, are small. This result contrasts with models that employ alternate finite-differencing schemes (Yamasaki 1968, Rosenthal 1970*a*). In these models, truncation errors associated with the space differencing provide a significant dissipation of kinetic energy. The absence of such a *numerical* dissipation in this model necessitates a larger *explicit* dissipation through the eddy viscosity coefficient. The important components of the energy budget are also shown in figure 9. The dissipation due to horizontal eddies is about half that due to vertical eddies, which includes dissipation at the surface. The values of the components are reasonable compared to observations and to symmetric model results. (See Anthes 1971 for a summary of empirical results.)

d. The Development of the Asymmetric Stage

This subsection discusses the development and maintenance of the asymmetric features of the circulation using the current (experiment 6) version of the model. A measure of the asymmetry is the standard deviation (from the circular mean) of any variable. Figure 10 shows the time variation of the standard deviations (SD) of the tangential and radial wind components and of the temperature in the upper level at a radius of 105 km. The early part of the storm's history is quite symmetric, with maximum SD of the wind components about 0.3 m/s and for the temperature about 0.05°C. The storm becomes quite asymmetric after 60 hr. Thereafter, SD for the wind components are about equal in magnitude to the azimuthal means at this level. However, the temperature field remains relatively symmetric even during the later stages, with SD rarely exceeding 1°C. This relative symmetry may be, in part, due to the symmetric boundary conditions on temperature.

Detailed analysis of the development of the asymmetries (Trout and Anthes 1971) shows that during the symmetric stage, when the variance of any quantity is small, wave number 4 accounts for nearly all of the variance. Because of the orientation of wave number 4 with respect to the four irregular corners of the grid, this early symmetry is probably due solely to the artificial aspects of the irregular boundary. Subsequent to the rapid growth of the variance, however, wave numbers 1 and 2 become dominant and account for most of the variance, in agreement with observations (Black and Anthes 1971). See Trout and Anthes (1971) for further details.

The appearance in the model storms of large-scale asymmetries that develop from initially axisymmetric conditions raises at least three questions: (1) What is the source of the initial perturbations? (2) Why do certain wavelengths become predominant? (3) What is the mechanism for growth of these disturbances? The next subsections present results from two types of initial perturbations and show that the initial form of the perturbations is

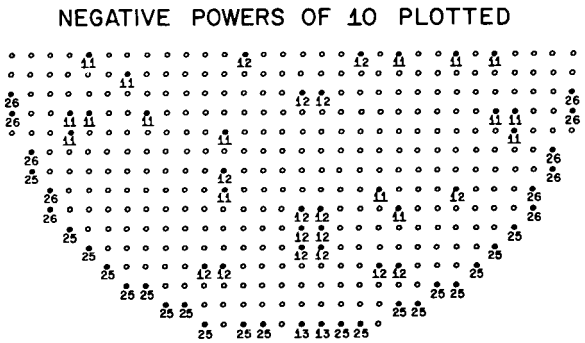

FIGURE 11.—Asymmetries in the v-component after one time step in the preliminary experiment ($|V_{i,j}|-|V_{31-i,31-j}|$ where $i=1,15$ and $j=1,30$). These asymmetries are due to truncation and roundoff errors alone and are functions of the grid system and the finite-difference scheme.

unimportant in determining the dominant scale of the asymmetries. The growth of the initially small disturbances is shown to be a type of dynamic (or inertial) instability in which longer wavelengths are more unstable than the shorter wavelengths. The important mechanism for the growth of the eddies is the barotropic conversion of mean azimuthal kinetic energy to eddy kinetic energy.

e. The Initial Perturbations

The initial asymmetries in experiment I and in the experiments discussed so far in this paper arise from nonsymmetric truncation and roundoff errors in the finite-difference schemes. On a 30×30 rectangular grid, a circularly symmetric field, α, with center at coordinate ($i=15.5$, $j=15.5$) obeys the symmetry relation $\alpha_{i,j}=\alpha_{31-i,31-j}$ for $i,j=1, 2, 3, \ldots 30$. Therefore, the difference $(\alpha_{i,j}-\alpha_{31-i,31-j})$ is a measure of the magnitude of the asymmetry, and $2(\alpha_{i,j}-\alpha_{31-i,31-j})/(\alpha_{i,j}+\alpha_{31-i,31-j})$ expresses the asymmetry as a percentage of the mean flow. The initial asymmetries in the wind field (fig. 11) after one time step are (in experiment I) on the order of 10^{-10} percent on the interior of the grid and 10^{-25} percent on the boundaries. Inspection of each term in the forecast equations showed these asymmetries to arise from the divergence terms in the continuity equation.

The magnitude and distribution of the initial perturbations, and consequently the time required for the disturbances to manifest themselves in the large-scale flow, varies with the grid and finite-difference scheme. The asymmetric stage begins at 120 hr for the nonstaggered grid, at 100 hr for the S1 grid, and at 60 hr for the S2 grid.

Although truncation errors produce perturbations that eventually grow to the interesting asymmetric features of the model, it is more appealing to deliberately introduce perturbations of known amplitude and variance. Therefore, initial asymmetries on the order of 10^{-1} percent (10 orders of magnitude greater than the perturbations due to truncation errors) were introduced by adding random numbers to the initial u and v components. As shown in figure 3, the asymmetric stage is reached much earlier (60 hr rather than 100 hr) with the greater amplitude perturbations. (The onset of the asymmetric stage is marked in fig. 3 by the rise in minimum pressure preceeding the oscillations in the pressure.) It is important to note, however, that during the asymmetric stage the structures of the model experiments are very similar (see also table 1), indicating that *the form of the random initial asymmetries is unimportant in determining the ultimate structure of the asymmetric circulation.* This conclusion, of course, refers only to the small amplitude, random noise associated with the model and does not apply to natural storms in which large-scale asymmetries in the environmental flow may be quite important in determining the storm's asymmetric structure.

f. Role of Dynamic Instability in the Development of the Asymmetries

The theory of dynamic instability has been investigated by many individuals over the years. The reader is referred to Kuo (1949), Godson (1950), and Van Mieghem (1951) for a review and discussion of the generalized concept of dynamic instability.

In the application of dynamic instability to the hurricane problem, meteorologists have generally referred to the growth of symmetric radial displacements in an axisymmetric vortex (Sawyer 1947, Alaka 1963, Yanai 1964, Yanai and Tokioka 1969). However, this instability, defined by the criterion

$$\left(\frac{\partial r\overline{v_\lambda}}{r\partial r}+f\right)\overline{Z}<0 \tag{24}$$

wheer

$$Z=\left(\frac{2v_\lambda}{r}+f\right),$$

v_λ is the tangential wind, and the $(\overline{\ })$ operator refers to an azimuthal average, does not appear to play an important role in the intensification of symmetric model storms (Yamasaki 1968, Ooyama 1969, Rosenthal 1969).

A second type of dynamic instability that seems relevant in the asymmetric hurricane model is the instability represented by the growth of azimuthal perturbations at the expense of the axisymmetric flow. For purely horizontal, nondivergent flow, a necessary and sufficient criterion is that

$$\frac{\partial}{\partial r}\left(\frac{\partial rv_\lambda}{r\partial r}+f\right)=0 \tag{25}$$

somewhere in the domain (Kuo 1949). However, the derivation of eq 25 requires that the horizontal perturbations vanish at the outer boundary, which is not strictly the case in the model in which the winds on the boundaries vary through the extrapolation procedure discussed earlier (subsec. 2f).

It may also be shown that, for nondivergent, horizontal flow, eq (24) is a sufficient criterion for the growth of azimuthal perturbations regardless of the form of the perturbations on the boundary.

In experiment 6 (the current version of the model), we have considered the criterion defined by eq (24) and (25).

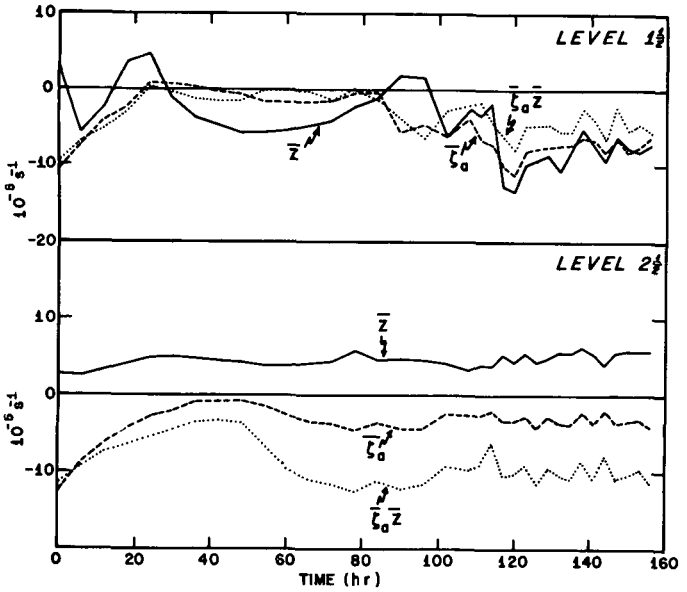

FIGURE 12.—Time variation of minimum azimuthal averages of $\bar{\zeta}_a, \bar{Z}$, and $\bar{\zeta}_a\bar{Z}$ for levels 1½ and 2½ in experiment 6.

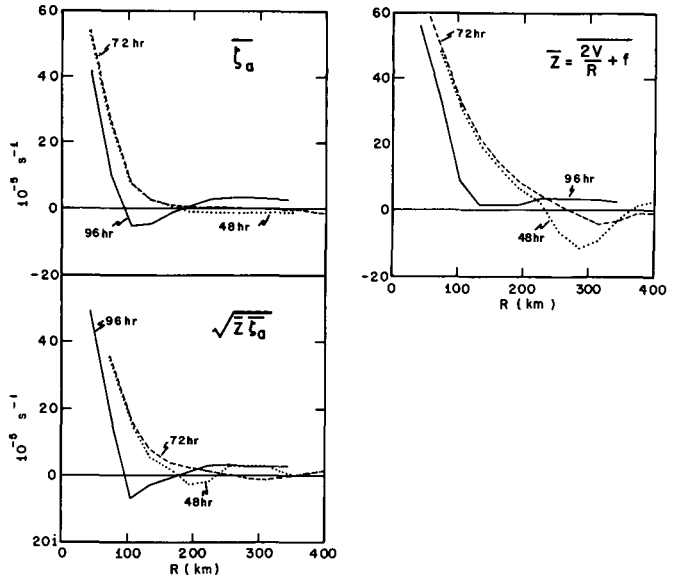

FIGURE 13.—Radial profiles of $\bar{\zeta}_a$, $\bar{Z}$, and $\sqrt{\bar{\zeta}_a\bar{Z}}$ at 48, 72, and 96 hr of experiment 6.

Figure 12 shows the time variation of the minimum azimuthal averages of ζ_a, Z, and the minimum value of the product, $\bar{\zeta}_a\bar{Z}$, for the upper (level 1½) and middle (level 2½) tropospheric layers. Negative absolute vorticity is present in the initial conditions at both levels beyond 300-km radius. During the first 40 hr, this outer area of negative ζ_a decreases in intensity in both layers. After about 48 hr, a new region of negative ζ_a appears close to the storm center at a radius of about 150 km. This inner region persists for the remainder of the forecast.

Figure 12 also shows that negative azimuthal averages of Z exist in level 1½, but never at level 2½ where the flow is always cyclonic. There are regions in both levels where the product is negative, thus the criterion in eq (24) is satisfied in both levels over most of the forecast period.

Although the asymmetries at level 1½ have been emphasized, there is significant eddy kinetic energy present in the middle tropospheric layer as well. The mean radial pressure gradient and the mean tangential flow are much stronger at this level, however, so that the asymmetric portion of the flow is a smaller percentage of the mean flow. The strong, symmetric pressure gradient force at this level is undoubtedly resisting the development of the azimuthal perturbations to a greater extent than the weaker pressure field in the outflow layer.

Figure 13 shows radial profiles of $\bar{Z}$, $\bar{\zeta}_a$, and $\bar{\zeta}_a\bar{Z}$ for selected times at level 1½. All the profiles have a minimum in absolute vorticity, so that eq (25) is also satisfied during the forecast. We next investigate the generation of the negative vorticity near the center. The vorticity equation in σ-coordinates may be written

$$\frac{d\zeta_a}{dt}=D+T+F \tag{26}$$

where the divergence term, D, is

$$D=-\zeta_a\nabla\cdot\mathbf{V}, \tag{27}$$

the tilting term, T, is

$$T=\frac{\partial\dot{\sigma}}{\partial y}\frac{\partial u}{\partial\sigma}-\frac{\partial\dot{\sigma}}{\partial x}\frac{\partial v}{\partial\sigma}, \tag{28}$$

and the friction term, F, is

$$F=\frac{\partial F(v)}{\partial x}-\frac{\partial F(u)}{\partial y}. \tag{29}$$

In eq (29), $F(v)$ and $F(u)$ represent the vertical and horizontal friction terms for the v and u components, respectively. Given an initially positive absolute voricity pattern, the divergence term by itself cannot produce negative ζ_a. Production of negative ζ_a must come from the tilting term, T. Figure 14 shows minimum (maximum negative) azimuthal averages of D, T, and the sum, $(D+T)$. The friction term, F, was also computed, and was much smaller in magnitude than either D or T. The terms in eq (27)–(29) were computed by interpolating the velocity components to the σ-levels and approximating the derivatives with centered differences. Figure 14 shows that both the divergence and tilting term contribute to the negative tendency. The spatial distributions of the minimums of T and D reveal that the minimum (maximum negative) divergence term occurs very close to the vortex center where the vorticity is large and positive and the divergence is maximum. The tilting term minimum occurs farther out, beyond the radius of maximum upward motion, where $\partial\dot{\sigma}/\partial r>0$. (For a symmetric vortex, $T=-(\partial\dot{\sigma}/\partial r)(\partial v_\lambda/\partial\sigma)$ and since $\partial v_\lambda/\partial\sigma$ is positive in the hurricane, the negative contribution occurs with $\partial\dot{\sigma}/\partial r>0$.)

The production of negative ζ_a may be physically interpreted from angular momentum considerations, where the angular momentum, M, is defined by

$$M=rv_\lambda+\tfrac{1}{2}fr^2 \tag{30}$$

and

$$\bar{\zeta}_a=\frac{\partial\bar{M}}{r\partial r}. \tag{31}$$

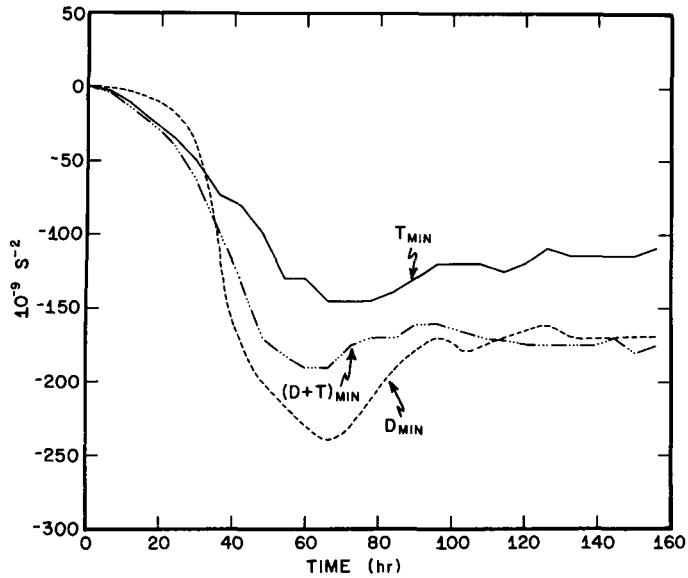

FIGURE 14.—Time variation of minimum azimuthal averages of divergence term (D), tilting term (T), and sum ($D + T$) in the vorticity equation at level 2 for experiment 6.

In the early stages of cyclone development M increases radially outward. The reversal of the radial gradient of M (production of negative ζ_a) may occur as air at large distances (high M) is advected inward in the boundary layer. When this air is ultimately carried upward in the narrow ring of ascent near the center of the vortex, it may, in spite of some frictional loss to the sea surface, retain a higher value of M than air at the same level but at a larger radial distance. The air at larger distances, in the middle levels, experiences little radial or vertical motion as shown by the middle level trajectory in figure 5.

In summary, substantial regions of negative absolute vorticity are produced in the middle and upper tropospheric layers through the tilting term in the vorticity equation. Both criteria for the development of azimuthal perturbations (in horizontal, nondivergent flow) are satisfied throughout the integration. Preference for the growth of longer waves (wave numbers 1 and 2) is probably the result of the selective effects of static stability in the presence of horizontal divergence (Houghton and Young 1970).

g. Eddy Kinetic Energy Budget

The eddy kinetic energy equation may be derived by forming the equation for the azimuthal mean kinetic energy and subtracting this equation from the total kinetic energy equation. The resulting equation is

$$\frac{\partial \overline{k_e}}{\partial t}=C_H+C_V+B+F \tag{32}$$

where the eddy kinetic energy is defined as

$$\overline{k_e}\equiv\frac{\overline{u'^2}+\overline{v'^2}}{2} \tag{33}$$

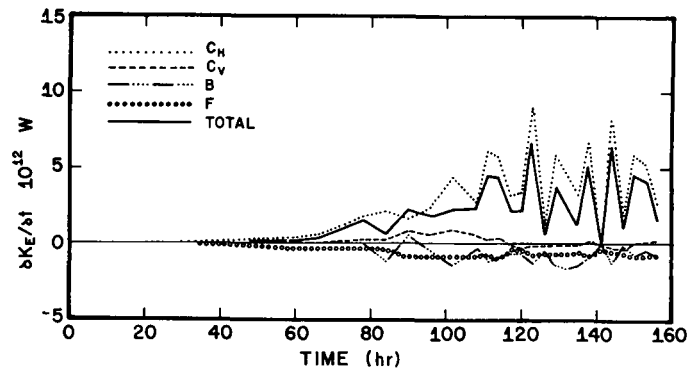

FIGURE 15.—Time variation of total eddy kinetic energy budget. C_H represents the conversion of azimuthal mean to eddy kinetic energy through horizontal, barotropic processes; C_V represents the effects of vertical eddies; B represents baroclinic effects; and F represents frictional effects. See subsection 3g for discussion of these terms.

and

$$C_H=-\overline{v_r'^2}\frac{\partial \overline{v_r}}{\partial r}+\overline{v_r'v_\lambda'}\left(\frac{2\overline{v_\lambda}}{r}-\frac{\partial r\overline{v_\lambda}}{r\partial r}\right)-\frac{\overline{v_r}\,\overline{v_\lambda'^2}}{r}, \tag{34}$$

$$C_V=-\overline{\dot{\sigma}'v_r'}\frac{\partial \overline{v_r}}{\partial \sigma}-\overline{\dot{\sigma}'v_\lambda'}\frac{\partial \overline{v_\lambda}}{\partial \sigma}, \tag{35}$$

$$B=-\overline{\frac{v_\lambda'}{r}\frac{\partial \phi'}{\partial \lambda}}-\overline{v_r'\frac{\partial \phi'}{\partial r}}-\left(\frac{\overline{RT}}{P}\right)\overline{\left(v_r'\frac{\partial p'}{\partial r}+\frac{v_\lambda'}{r}\frac{\partial \overline{p}'}{\partial \lambda}\right)}$$
$$-\overline{\left(\frac{RT}{P}\right)'\left(v_r'\frac{\partial p'}{\partial r}+\frac{v_\lambda'}{r}\frac{\partial p'}{\partial \lambda}\right)}-\overline{\left(\frac{RT}{P}\right)'u'\frac{\partial \overline{p}}{\partial r}}, \tag{36}$$

and

$$F=\overline{v_r'F_r'}+\overline{v_\lambda'F_\lambda'}. \tag{37}$$

The term C_H represents the conversion of mean to eddy kinetic energy through horizontal, barotropic processes, and should be the predominant source of energy for the eddies if dynamic instability is the important mechanism in the eddy generation. The term C_V represents the effect of vertical eddies. The term B represents baroclinic effects and would be predominant if baroclinic instability were important. (The last two terms in B are several orders of magnitude smaller than the first three terms.) Finally, F represents the effects of asymmetries in the parameterization of the subgrid-scale eddy stresses.

Figure 15 shows the time variation of the volume integral of k_e, defined by

$$K_e=-\frac{2\pi}{g}\int_0^{R_m} r\int_1^0 \frac{\partial k_e}{\partial t}p^*d\sigma dr \tag{38}$$

where R_m is the edge of the domain (about 440 km). Because the computation of the various terms in eq (34)–(37) require interpolation in the vertical, as well as from the Cartesian grid to a polar coordinate grid, the values shown in figure 15 should be considered approximate.

Figure 15 shows that the significant positive contribution to the eddy kinetic energy is C_H, representing the barotropic conversion of mean to eddy kinetic energy, and provides strong support for the hypothesis that dynamic

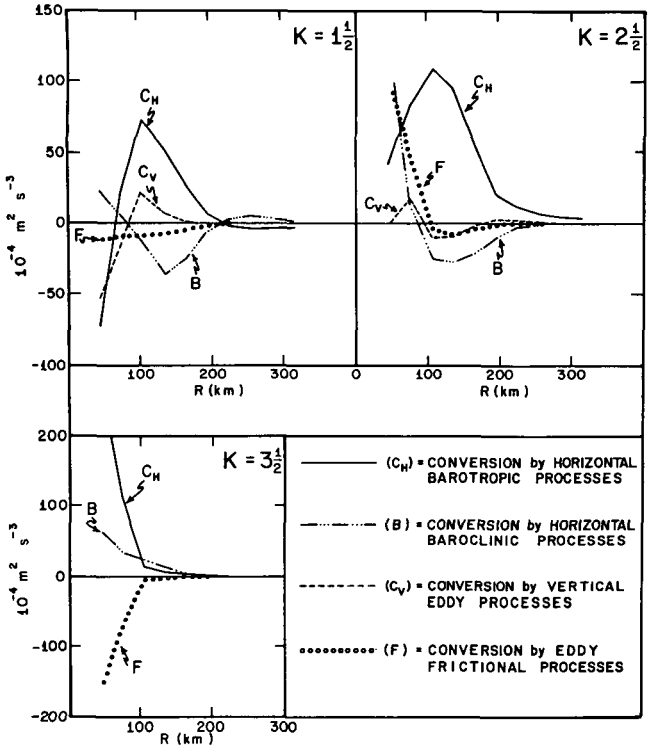

FIGURE 16.—Radial profiles of terms in eddy kinetic energy budget at 138 hr in experiment 6.

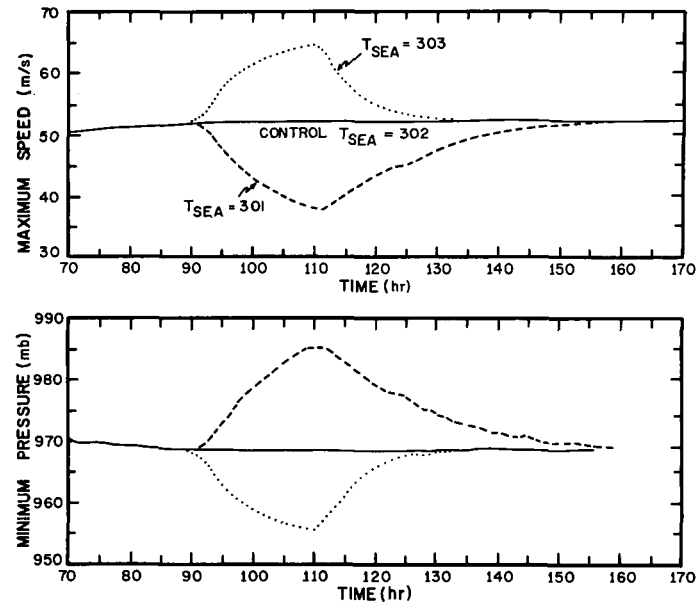

FIGURE 17.—Effect of increasing and decreasing sea temperature by 1°C on maximum wind speed and minimum pressure for symmetric analog.

instability is present in the model. The vertical eddy term, C_V, is slightly positive at first, then slightly negative toward the end of the forecast. The baroclinic term, B, and the friction term, F, are negative throughout the forecast.

The eddy kinetic energy budget establishes dynamic, or inertial, instability as the mechanism for the breakdown in symmetry and the development of large-scale eddies in the outflow layer. These eddies continually extract kinetic energy from the mean circulation. The mean kinetic energy is maintained through the low-level, cross-isobar flow associated with the mean meridional circulation and the upward transport of kinetic energy by the rising motion near the center of the storm.

Figure 16 shows radial profiles of the various terms in the eddy kinetic energy equation at a typical time (138 hr) during the forecast. The terms are less reliable near the origin where the errors associated with the interpolation to the polar grid are maximum. From figure 16, we see that the maximum conversion occurs around 100 km. The baroclinic processes consume eddy kinetic energy in the middle and upper troposphere. The slight positive contribution by baroclinic processes in the boundary layer *may* be associated with the generation of eddy kinetic energy on the scale of the spiral bands.

h. Increase of Sea Temperature in One Quadrant

Empirical results (Palmén 1948, Miller 1957, Perlroth 1962) and symmetric hurricane model calculations (Ooyama 1968) indicate a strong relationship between sea-surface temperature and hurricane intensity. Figure 17 shows the effect of varying the sea-surface temperature over a 2°C range for 20 hr on the symmetric analog. The immediate response and the total range of 26 m/s in the maximum wind speed confirms the sensitivity of the hurricane to small variations in sea-surface temperature.

In addition to the recognized importance of the sea-surface temperature to the intensity of the storm, it is sometimes suggested that horizontal sea-temperature gradients may also affect the storm's motion, perhaps through a differential enhancement of convective latent heat release. Although the looping motion of the asymmetric model storm is small and poorly understood, it does afford the opportunity for at least a crude experiment to investigate the effect, if any, of sea-surface temperature differences on the storm's motion.

Figure 18 shows the effect of raising the sea temperature from 302° to 303°K in the "northeast" quadrant of the grid over the last 30 hr of experiment 6. The sea temperature over the rest of the grid remains unchanged. The position of the storm center at 136 hr, shown in figure 8, is in the "northwest" quadrant where the temperature is constant. As the storm moves over the warmer water (at about 140 hr), an increase in intensity occurs, reaching a maximum at about 146 hr when the wind speed is about 6 m/s greater than that of the control. As the storm moves back over colder water, the differences from the control become less.

If the differing sea temperature field does affect the storm motion, one would expect at least a small change in speed or direction as the storm moved over the warmer water. There was, however, no discernible change in the motion of the storm despite a considerable (10 percent)

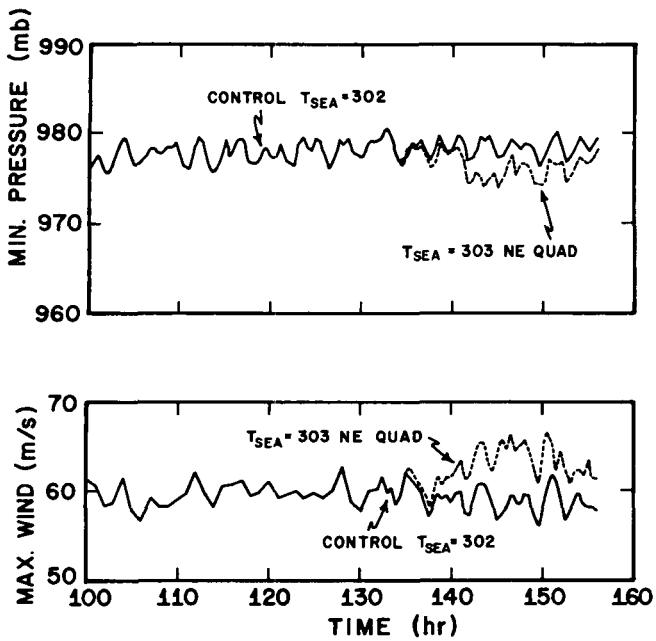

FIGURE 18.—Effect of increasing sea temperature by 1°C in northeast quadrant alone for asymmetric model, experiment 6.

change in the storm's intensity. This result suggests, although by no means proves, that storm *motion* is not appreciably affected by horizontal temperature gradients in the sea temperature.

4. SUMMARY AND CONCLUSIONS

Additional experiments with an improved version of an isolated, asymmetric model of the tropical cyclone are described. Increased horizontal resolution is achieved through the horizontal staggering of the variables. An explicit water vapor cycle is included that enables the study of the hurricane's water vapor budget and the simulation of nonconvective heat release. The modeling of the horizontal diffusion of heat, water vapor, and momentum is considered more realistic in the current version of the model.

The development of the asymmetric structure of the model hurricane is examined in considerable detail. The asymmetries in the outflow layer are shown to result from dynamic instability, with the source of eddy kinetic energy being the mean azimuthal flow.

Well-defined spiral bands of convective heat release occur in these experiments. These bands propagate outward at a speed of about 24 kt and compare favorably in structure with outer rainbands in nature.

An anticyclonic looping of the vortex center is observed during the later stages of these experiments. Although the mechanism for this motion is not clear, the looping seems to be closely associated with the asymmetries in the upper level circulation.

The intensity of the model is found to be sensitive to the sea-surface temperature, in agreement with previous results. However, the looping motion of the storm is *not* noticeably affected as the storm passes over water of varying temperature.

The structure of the model storm and the components of the energy budget agree quite well with empirical results and with previous symmetric model results in spite of the coarse vertical and horizontal resolution.

APPENDIX: FINITE-DIFFERENCE EQUATIONS

Finite-Difference Equations for Staggered Grid S1

In the appendix, the following notation will be used (Shuman and Stackpole 1968):

$$\alpha_x \equiv \frac{\alpha_{i,\,j+1/2}-\alpha_{i,\,j-1/2}}{\Delta x}$$

$$\bar{\alpha}^x \equiv \frac{\alpha_{i,\,j+1/2}+\alpha_{i,\,j-1/2}}{2}$$

$$\alpha_y \equiv \frac{\alpha_{i+1/2,\,j}-\alpha_{i-1/2,\,j}}{\Delta y}$$

and (39)

$$\bar{\alpha}^y \equiv \frac{\alpha_{i+1/2,\,j}+\alpha_{i-1/2,\,j}}{2}$$

where j is the east–west index and i is the north–south index.

We also introduce the following four-point operators:

$$\bar{\bar{\alpha}}^y \equiv \frac{\alpha_{i+1,\,j}+2\alpha_{i,\,j}+\alpha_{i-1,\,j}}{4}$$

and (40)

$$\bar{\bar{\alpha}}^x \equiv \frac{\alpha_{i,\,j+1}+2\alpha_{i,\,j}+\alpha_{i,\,j-1}}{4}.$$

For vertical differences and averages, we define

$$\bar{\alpha}^\sigma \equiv \frac{(\alpha_{k+1/2}+\alpha_{k-1/2})}{2}$$

and (41)

$$\delta\alpha \equiv (\alpha_{k+1/2}-\alpha_{k-1/2}).$$

The finite-difference equations associated with staggered grid S1 for the u- and v-component equations of motion are

$$\frac{\partial p^*u}{\partial t} \approx -(\bar{u}^x\overline{\overline{p^*u}}^{\,x})_x-(\bar{u}^y\overline{\overline{p^*v}}^{\,y})_y-\frac{\overline{\delta\dot{\sigma}}^{xy}\overline{p^*u}^\sigma}{\delta\sigma}-\overline{p^*}^{xy}\overline{\overline{\phi_x}}^{\,y}$$
$$-R\overline{T}^{xy}\overline{p^*_x}^{\,y}+fp^*v+[K_H(p^*u)_x]_x+[K_H(p^*u)_y]_y+F_V(u) \tag{42}$$

and

$$\frac{\partial p^*v}{\partial t} \approx -(\bar{v}^x\overline{\overline{p^*u}}^{\,x})_x-(\bar{v}^y\overline{\overline{p^*v}}^{\,y})_y-\frac{\overline{\delta\dot{\sigma}}^{xy}\overline{p^*v}^\sigma}{\delta\sigma}$$
$$-\overline{p^*}^{xy}\overline{\overline{\phi_y}}^{\,x}-R\overline{T}^{xy}\overline{p^*_y}^{\,x}-fp^*u$$
$$+[K_H(p^*v)_x]_x+[K_H(p^*v)_y]_y+F_V(v) \tag{43}$$

where the finite-difference analogs for the vertical friction terms, $F_V(u)$ and $F_V(v)$, are given in eq (6). In this sec-

tion, the terms (p^*u) and (p^*v) represent $(u\overline{p^*}^{xy})$ and $(v\overline{p^*}^{xy})$, respectively.

The analogs for the continuity and thermodynamic equations are

$$\frac{\partial p^*}{\partial t} \approx -(\overline{p^*u})^y_x - (\overline{p^*v})^x_y - p^* \frac{\delta\dot{\sigma}}{\delta\sigma} \tag{44}$$

and

$$\frac{\partial p^*T}{\partial t} \approx -(\overline{p^*u}^y \overline{T}^x)_x - (\overline{p^*v}^x \overline{T}^y)_y - p^* \frac{\delta\dot{\sigma}\overline{T}^\sigma}{\delta\sigma}$$
$$+\frac{RT\omega}{c_p\sigma} + \frac{p^*}{c_p}\dot{Q} + p^*[K_T(T)_x]_x + p^*[K_T(T)_y]_y \tag{45}$$

with the finite-difference form for ω given by

$$\omega = \frac{dp}{dt} = p^*\dot{\sigma} + \sigma\frac{dp^*}{dt}$$
$$\approx p^*\overline{\dot{\sigma}}^\sigma + \overline{\sigma}^\sigma\left(\frac{\partial p^*}{\partial t} + \overline{u}^{xy}\overline{p^*}^x_x + \overline{v}^{xy}\overline{p^*}^y_y\right) \tag{46}$$

As in paper I, the notation $\overline{T}^\sigma$ in eq (45) signifies that *potential* temperature, rather than temperature itself, is linearly interpolated between σ-levels.

The finite-difference analogs for the horizontal derivatives in the water vapor forecast are analogous to the equation for temperature and are not given.

In eq (42) and (43), the use of the four-point averaging operator is necessary if the finite-difference equations are to conserve kinetic energy. The kinetic energy equation for this system may be written

$$\frac{\partial\overline{p^*}^{xy}k}{\partial t} + k\left(\frac{\partial\overline{p^*}^{xy}}{\partial t} + \nabla\cdot\overline{p^*}^{xy}\mathbf{V}\right) + \nabla\cdot\overline{p^*}^{xy}\mathbf{V}k$$
$$+\overline{p^*}^{xy}\mathbf{V}\cdot\frac{\delta\dot{\sigma}\mathbf{V}}{\delta\sigma} = -\mathbf{V}\cdot(\overline{p^*}^{xy}\nabla\phi + R\overline{T}^{xy}\nabla p^*). \tag{47}$$

For conservation of kinetic energy, k, the part of the finite-difference analogs to the horizontal momentum flux terms that yield the $\nabla\cdot\overline{p^*}^{xy}\mathbf{V}$ term in eq (47) must cancel with $\partial\overline{p^*}^{xy}/\partial t$ as computed from the finite-difference analog to the continuity equation. Consider the u-component equation (in one dimension for simplicity)

$$\frac{\partial p^*u}{\partial t} = -\frac{\partial p^*uu}{\partial x}, \tag{48}$$

which may be written, analytically,

$$p^*\frac{\partial u}{\partial t} + u\frac{\partial p^*}{\partial t} = -p^*u\frac{\partial u}{\partial x} - u\frac{\partial p^*u}{\partial x}. \tag{49}$$

In the exact, differential equation, the cancellation of $u(\partial p^*/\partial t)$ with $-u(\partial p^*u/\partial x)$ by the continuity equation is necessary for the conservation of kinetic energy. For any finite-difference analog to eq (48),

$$\frac{\delta\overline{p^*}^{xy}u}{\delta t} = -\frac{\delta\overline{p^*}^{xy}uu}{\delta x}. \tag{50}$$

It is also necessary that the part of $\delta\overline{p^*}^{xy}uu/\delta x$ corresponding to $u(\delta\overline{p^*}^{xy}u/\delta x)$ cancel with the part of $\delta\overline{p^*}^{xy}u/\delta t$ corresponding to $u(\delta\overline{p^*}^{xy}/\delta t)$ as computed from the continuity equation. One may verify by substitution that the four-point averaging operator yields this necessary cancellation with the continuity equation.

Finite-Difference Equations for Staggered Grid S2

The finite-difference analogs associated with staggered grid S2 are derived by Lilly (1965) and tested as Scheme C by Grammeltvedt (1969). For the equations of motion, the analogs are

$$\frac{\partial p^*u}{\partial t} \approx -[\overline{u}^x(\overline{p^*u})^x]_x - [\overline{u}^y(\overline{p^*v})^x]_y - p^*\frac{\delta\dot{\sigma}^x\overline{u}^\sigma}{\delta\sigma}$$
$$-\overline{p^*}^x\overline{\phi}^\sigma_x - R\overline{T}^x p^*_x + f(\overline{p^*v}^{xy}) \tag{51}$$

and

$$\frac{\partial p^*v}{\partial t} \approx -[\overline{v}^x(\overline{p^*u})^y]_x - [\overline{v}^y(\overline{p^*v})^y]_y - p^*\frac{\delta\dot{\sigma}^y\overline{v}^\sigma}{\delta\sigma}$$
$$-\overline{p^*}^y\overline{\phi}^\sigma_y - R\overline{T}^y p^*_y - f(\overline{p^*u})^{xy}. \tag{52}$$

The friction terms are the same as those in eq (42) and (43) and are not repeated. In this section, the terms (p^*u) and (p^*v) represent $\overline{p^*}^x u$ and $\overline{p^*}^y v$, respectively.

The continuity and thermodynamic equations in this scheme are

$$\frac{\partial p^*}{\partial t} \approx -(p^*u)_x - (p^*v)_y - p^*\frac{\delta\dot{\sigma}}{\delta\sigma} \tag{53}$$

and

$$\frac{\partial p^*T}{\partial t} \approx -[\overline{T}^x(p^*u)]_x - [\overline{T}^y(p^*v)]_y + \frac{RT\omega}{c_p\sigma} + \cdots\cdots \tag{54}$$

where

$$\omega \approx p^*\overline{\dot{\sigma}}^\sigma + \overline{\sigma}^\sigma\left(\frac{\partial p^*}{\partial t} + \overline{u}^x\overline{p^*}^x_x + \overline{v}^y\overline{p^*}^y_y\right). \tag{55}$$

The remaining terms in eq (54) are the same as those in eq (45). This scheme also conserves total energy (Lilly 1965).

ACKNOWLEDGMENTS

Rapid progress with The National Hurricane Research Laboratory asymmetric hurricane model would not have been possible without the firm background work with the symmetric model by the head of the theoretical studies group, Stanley L. Rosenthal. His support and suggestions concerning this work is gratefully acknowledged.

James Trout aided substantially in the programming of various aspects of the current model. Robert Carrodus and Charles True were responsible for the figures, and Mary Jane Clarke and Kandie Baluch typed the manuscript.

REFERENCES

Alaka, Michael A., "Instability Aspects of Hurricane Genesis," *National Hurricane Research Project Report* No. 64, U.S. Department of Commerce, Weather Bureau, Miami, Fla., June **1963**, 23 pp.

Anthes, Richard A., "A Numerical Model of the Slowly Varying Tropical Cyclone in Isentropic Coordinates," *Monthly Weather Review*, Vol. 99, No. 8, Aug. **1971**, pp. 617–635.

Anthes, Richard A., "Non-Developing Experiments With a Three-Level Axisymmetric Hurricane Model," *NOAA Technical Memorandum* ERL NHRL-97, U.S. Department of Commerce, National Hurricane Research Laboratory, Coral Gables, Fla., Jan. **1972**, 18 pp.

Anthes, Richard A., Rosenthal, Stanley L., and Trout, James W., "Preliminary Results From an Asymmetric Model of the Tropical Cyclone," *Monthly Weather Review*, Vol. 99, No. 10, Oct. **1971***a*, pp. 744–758.

Anthes, Richard A., Trout, James W., and Ostlund, Stellan S., "Three Dimensional Particle Trajectories in a Model Hurricane," *Weatherwise*, Vol. 24, No. 4, Aug. **1971***b*, pp. 174–178.

Anthes, Richard A., Trout, James W., and Rosenthal, Stanley L., "Comparisons of Tropical Cyclone Simulations With and Without the Assumption of Circular Symmetry," *Monthly Weather Review*, Vol. 99, No. 10, Oct. **1971***c*, pp. 759–766.

Black, Peter G., and Anthes, Richard A., "On the Asymmetric Structure of the Tropical Cyclone Outflow Layer," *Journal of the Atmospheric Sciences*, Vol. 28, No. 8, Nov. **1971**, pp. 1348–1366.

Charney, Jule G., and Eliassen, Arnt, "On the Growth of the Hurricane Depression," *Journal of the Atmospheric Sciences*, Vol. 21, No. 1, Jan. **1964**, pp. 68–75.

Charney, Jule G., "Tropical Cyclogenesis and the Formation of the Intertropical Convergence Zone," *Summer Seminar in Applied Mathematics, Lectures in Applied Mathematics, Troy, N.Y., July 6–31, 1970*, Vol. 13, American Mathematical Society, Providence, R.I., **1971**, pp. 355–368.

Gentry, R. Cecil, "A Study of Hurricane Rainbands," *National Hurricane Research Project Report* No. 69, U.S. Department of Commerce, Weather Bureau, Miami, Fla., Mar. **1964**, 85 pp.

Godson, Warren L., "Generalized Criteria for Dynamic Instability," *Journal of Meteorology*, Vol. 7, No. 4, Aug. **1950**, pp. 268–278.

Grammeltvedt, Arne, "A Survey of Finite-Difference Schemes for the Primitive Equations for a Barotropic Fluid," *Monthly Weather Review*, Vol. 97, No. 5, May **1969**, pp. 384–404.

Hawkins, Harry F., and Rubsam, Daryl T., "Hurricane Hilda, 1964: II. Structure and Budgets of the Hurricane on October 1, 1964," *Monthly Weather Review*, Vol. 96, No. 9, Sept. **1968**, pp. 617–636.

Houghton, David D., and Young, John A., "A Note on Inertial Instability," *Tellus*, Vol. 22, No. 5, Stockholm, Sweden, **1970**, pp. 581–583.

Kuo, Hsiao-Lan, "Dynamic Instability of Two-Dimensional Nondivergent Flow in a Barotropic Atmosphere," *Journal of Meteorology*, Vol. 6, No. 2, Apr. **1949**, pp. 105–122.

Kurihara, Yoshio, and Holloway, J. Leith, Jr., "Numerical Integration of a Nine-Level Global Primitive Equations Model Formulated by the Box Method," *Monthly Weather Review*, Vol. 95, No. 8, Aug. **1967**, pp. 509–530.

Lilly, Douglas K., "On the Computational Stability of Numerical Solutions of Time-Dependent Non-Linear Geophysical Fluid Dynamics Problems," *Monthly Weather Review*, Vol. 93, No. 1, Jan. **1965**, pp. 11–26.

Matsuno, Taroh, "Numerical Integrations of the Primitive Equations by a Simulated Backward Difference Method," *Journal of the Meteorological Society of Japan*, Ser. 2, Vol. 44, No. 1, Tokyo, Feb. **1966**, pp. 76–84.

Miller, Banner I., "On the Maximum Intensity of Hurricanes," *National Hurricane Research Project Report* No. 14, U.S. Department of Commerce, Weather Bureau, Miami, Fla., Dec. **1957**, 19 pp.

Ogura, Yoshimitsu, and Charney, Jule G., "A Numerical Model of Thermal Convection in the Atmosphere," *Proceedings of the International Symposium on Numerical Weather Prediction, Tokyo, Japan, November 7–13, 1960*, Meteorological Society of Japan, Tokyo, Mar. **1962**, pp. 431–451.

Ooyama, Katsuyuki, "Numerical Simulation of Hurricanes," *Proceedings of the First National Conference on Weather Modification, State University of New York, Albany, April 28–May 1, 1968*, American Meteorological Society, Boston, Mass., **1968**, pp. 129–135.

Ooyama, Katsuyuki, "Numerical Simulation of the Life Cycle of Tropical Cyclones," *Journal of the Atmospheric Sciences*, Vol. 26, No. 1, Jan. **1969**, pp. 3–40.

Palmén, Erik H., "On the Formation and Structure of Tropical Hurricanes," *Geophysica*, Vol. 3, No. 26, Helsinki, Finland, **1948**, pp. 26–38.

Perlroth, Irving, "Relationship of Central Pressure of Hurricane Esther (1961) and the Sea Surface Temperature Field," *Tellus*, Vol. 14, No. 4, Stockholm, Sweden, Nov. **1962**, pp. 404–408.

Phillips, Norman A., "A Coordinate System Having Some Special Advantages for Numerical Forecasting," *Journal of Meteorology*, Vol. 14, No. 2, Apr. **1957**, pp. 184–185.

Rosenthal, Stanley L., "Numerical Experiments With a Multilevel Primitive Equation Model Designed to Simulate the Development of Tropical Cyclones: Experiment I," *ESSA Technical Memorandum* ERLTM-NHRL 82, U.S. Department of Commerce, National Hurricane Research Laboratory, Miami, Fla., Jan. **1969**, 36 pp.

Rosenthal, Stanley L., "Experiments With a Numerical Model of Tropical Cyclone Development—Some Effects of Radial Resolution," *Monthly Weather Review*, Vol. 98, No. 2, Feb. **1970***a*, pp. 106–120.

Rosenthal, Stanley L., "A Circularly Symmetric Primitive Equation Model of Tropical Cyclone Development Containing an Explicit Water Vapor Cycle," *Monthly Weather Review*, Vol. 98, No. 9, Sept. **1970***b*, pp. 643–663.

Rosenthal, Stanley L., "The Response of a Tropical Cyclone Model to Variations in Boundary Layer Parameters, Initial Conditions, Lateral Boundary Conditions, and Domain Size," *Monthly Weather Review*, Vol. 99, No. 10, Oct. **1971**, pp. 767–777.

Sawyer, John Stanley, "Notes on the Theory of Tropical Cyclones," *Quarterly Journal of the Royal Meteorological Society*, Vol. 73, Nos. 315–316, London, England, Jan.–Apr. **1947**, pp. 101–126.

Senn, Harry V., and Stevens, J. A., "Radar Hurricane Research, Sept. 1, 1963–Aug. 1, 1964," *Final Report*, Contract No. Cwb-10755, Institute of Marine Science, University of Miami, Coral Gables, Fla., Aug. **1964**, 76 pp.

Shuman, Frederick G., and Stackpole, John D., "Note on the Formulation of Finite Difference Equations Incorporating a Map Scale Factor," *Monthly Weather Review*, Vol. 96, No. 3, Mar. **1968**, pp. 157–161.

Smagorinsky, Joseph, Manabe, Syukuro, and Holloway, J. Leith, Jr., "Numerical Results From a Nine-Level General Circulation Model of the Atmosphere," *Monthly Weather Review*, Vol. 93, No. 12, Dec. **1965**, pp. 727–768.

Sundqvist, Hilding, "Numerical Simulation of the Development of Tropical Cyclones With a Ten-Level Model, Part 1," *Tellus*, Vol. 22, No. 4, Stockholm, Sweden, **1970**, pp. 359–390.

Trout, James W., and Anthes, Richard A., "Horizontal Asymmetries in a Numerical Model of a Hurricane," *NOAA Technical Memorandum* ERL NHRL-93, U.S. Department of Commerce, National Hurricane Research Laboratory, Coral Gables, Fla., Nov. **1971**, 37 pp.

Van Mieghem, Jacques M., "Hydrodynamic Instability," *Compendium of Meteorology*, American Meteorological Society, Boston, Mass., **1951**, 1334 pp. (see pp. 434–453).

Yamasaki, Masanori, "Numerical Simulation of Tropical Cyclone Development With the Use of Primitive Equations," *Journal of the Meteorological Society of Japan*, Vol. 46, No. 3, Tokyo, June **1968**, pp. 178–201.

Yanai, Michio, "Formation of Tropical Cyclones," *Reviews of Geophysics*, Vol. 2, No. 2, May **1964**, pp. 367–414.

Yanai, Michio, and Tokioka, T., "Axially Symmetric Meridional Motions in the Baroclinic Circular Vortex: A Numerical Experiment," *Journal of the Meteorological Society of Japan*, Vol. 47, No. 3, Tokyo, June **1969**, pp. 183–198.

[*Received August 11, 1971; revised February 22, 1972*]